Compressive stiffness of staggered woodpile lattices: mechanics, measurement, and scaling laws

Enrique Cuan-Urquizo[a,b*], Faezeh Shalchy[b], Atul Bhaskar[b]

[a] *Tecnologico de Monterrey, Escuela de Ingeniería y Ciencias, Epigmenio González 500 Fracc. San Pablo, Querétaro, México 76130*
[b] *Faculty of Engineering and the Environment, Southampton Innovation Boldrewood Campus, University of Southampton, Southampton, SO16 7QF, UK*

Abstract

Lattices in woodpile arrangement are of interest in many applications such as tissue engineering scaffolds, elastic metamaterials and lightweight structures: the choice in lattice arrangement and stacking parameters facilitate innovative material design. Additive manufacturing has enabled fabrication of such structured materials with tunable properties. Here, the elastic response of woodpile lattices is studied analytically, numerically, and experimentally when they are compressed in the stacking direction, with struts staggered in alternating layers. Expressions for the apparent Young's modulus, and its dependence on porosity, are derived from the analysis of a periodically-supported, periodically-loaded, elastic filament. A fifth power law relating the apparent Young's modulus with the volume fraction is obtained in the asymptotic limit of high porosity, which is consistent with scaling arguments presented here. When the stacking is asymmetric, the apparent stiffness is presented in terms of an analytically known function of the skewness parameter α. For dense lattices, departure from the proposed power law is observed in computational simulations, as well as laboratory experiments on polylactic acid (PLA) 3D-printed woodpiles. Variations from power law can be attributed to unaccounted for effects in the micromechanics of the filaments, e.g. filament shear and diametrical compression. The experimentally obtained relationship, between the apparent modulus and porosity, is in excellent agreement with our analysis and numerical results.

Keywords: Lattice material, apparent elastic modulus, woodpile structure, 3D-printing

1. Introduction

Recent advances in additive manufacturing have enabled the fabrication of structured materials with properties that are usually not afforded by most naturally occur-

*Corresponding author

Email addresses: ecuanurqui at tec.mx (Enrique Cuan-Urquizo[a,b*]), f.shalchy at soton.ac.uk (Faezeh Shalchy[b]), a.bhaskar at soton.ac.uk (Atul Bhaskar[b])

ring homogeneous matter. Several promising lattice geometries are currently being explored, all with the aim to engineer designer materials with tunable properties [1, 2]. Of these, perhaps the simplest, yet easiest to fabricate by a filament extrusion based additive manufacturing process, is the so-called woodpile structure. Materials with structural hierarchy, in order to tailor their properties, have been proposed for a while [3]; their physical realisation has been helped by the advances in modern additive manufacturing. In this paper, we are concerned with elastic lattices composed of orthogonally stacked filaments in a woodpile arrangement. Such lattice structures are commonly used in biomedical scaffolds [4–7], electromagnetic bandgap structures [8–12], and other lightweight structural applications [13, 14]. Just as bandgap structures in electromagnetism and optics have led to a flurry of research activities, acoustic meta-materials with hierarchical lattice geometry appear promising for tailoring vibro-acoustic transmission of mechanical waves [15] . In the area of tissue engineering, woodpile scaffolds provide structural support for cell attachment and proliferation [16]. These scaffolds require a certain degree of interconnected porosity to enable cellular processes, whereas their mechanical properties are of great interest as they should be capable to withstand mechanical loading [17, 18]. Here we are interested in the elasticity of such lattice materials.

Significant simplification in the analysis of remotely loaded lattice structures can be made, thanks to the translational symmetry, as exploited previously by several authors in various contexts. Planar [19] and spatial [20] tensile networks have been analysed to determine the effective elastic moduli. Unusual properties such as negative apparent Poisson's ratio have been reported [21]. The classical result for 2D honeycombs was presented by Gibson and Ashby [22–24], who made use of the periodicity in hexagonal honeycombs to obtain analytical expressions for the in-plane stiffness. Bonfanti and Bhaskar [25–27] carried out non-linear elasto-plastic analysis of hexagonal honeycombs and other complex lattices in closed form and also presented a scaling argument for non-linear response of such lattices made with elastic-perfectly plastic material. Christensen [28] obtained elastic moduli of transversely isotropic solids in the limit of low density. They considered cellular geometry with *pentagonal dodecahedra* as the repetitive unit. Warner and Edwards [29] presented a scaling argument for the effective elastic modulus of cellular solids. The arguments in Ashby and Warner & Edwards can be summarised as follows. For honeycombs of cell wall thickness t and characteristic cell length λ, the apparent density scales as $\rho \sim (t/\lambda)$, whereas apparent modulus scales according to $\langle E\rangle \sim (t/\lambda)^3$ following simple flexural mechanics of cell walls combined with scaling of the apparent strain and the remote stress, resulting the a modulus-apparent density scaling as $\langle E\rangle \sim \rho^3$. These scaling relationships change for 3D open-cell lattices and foams as $\rho \sim (t/\lambda)^2$ and $\langle E\rangle \sim (t/\lambda)^4$ respectively, giving rise to $\langle E\rangle \sim \rho^2$. The precise constants of proportionality involved in these scaling laws have to be determined by detailed mechanics. As opposed to these, the woodpile lattice has characteristic length scale in the stacking direction as the diameter of the cylindrical struts, whereas that in each stacking layer is λ, the spacing between the struts. These differences result in very different modulus-porosity relationship, which is the subject of this work.

Despite a huge experimental interest in woodpile structures, review of the literature reveals that most studies are limited to computations or experimentation on structures

with *specific* lattice and material parameters; a general theoretical treatment of the mechanics of such elastic lattices is missing. Here, we systematically investigate the mechanical behaviour of woodpile structures under compression analytically, numerically and experimentally. Compressive stiffness, when alternate layers are stacked symmetrically or asymmetrically, is presented as a function of key architectural parameters. Analytical expressions for the apparent stiffness are valuable for *material design*, since the sensitivity to the parameters of the micro-structural architecture is then available.

The mechanics of such elastic lattices *along the filament direction* and when such slender lattice structures are in flexure have been recently studied [13, 30]. The dominant micromechanics in both these cases is the *stretch of the filaments*. Materials with micro-structure are frequently described by the apparent properties, which may be anisotropic depending on the lattice symmetry. Woodpile lattices are orthotropic because of the material symmetry about three orthogonal planes. Properties along the two filament axes are identical, which would be different from those along the stacking direction. Experimentally measured stiffness and strength in the stacking direction are significantly different from those in other two directions for 3D-printed lattice structures [31]. Review of the properties, structure, and processes for extrusion-based methods presented in [32]. Design methods for structures fabricated using extrusion based 3D-printing have been surveyed in [33]. Hutmacher et al. [34] reported the cellular response as well as compressive properties in the stacking direction of polycaprolactone (PCL) scaffolds fabricated using fused deposition modeling (FDM), when the alternative layers are not orthogonal. Zein et al. [35] characterised the stiffness and strength of PCL scaffolds under compression for various filament orientations. Miranda et al. [36, 37] studied calcium tissue engineering scaffolds using Finite Element (FE) simulations and laboratory experiments for various filament orientations. Naghieh et al. [38], studied the elastic response of FDM fabricated PLA specimens using FE simulations. The discrepancy, between numerical and experimental results observed in [38], was attributed to the effect of layer penetration between adjacent filaments. Norato et al. [39] proposed an analytical model to predict the apparent Young's modulus in the stacking direction. The dominant deformation considered in [39] is diametrical compression, which is valid for woodpiles with alternate layers aligned, as opposed to the staggered arrangement considered here.

In the field of tissue engineering, porous structures as well as architectured material have been used to provide interconnected internal structure for cells to grow [40]. Initially foam were used for such application [16], however with the advent of additive manufacturing, the use of structured material with controlled porosity is gaining popularity [41]. The effect of the relative position of the filament with respect to adjacent layers on the apparent properties of woodpile scaffolds was first studied experimentally by Sobral et al. [42]. Arrangements that possessed staggered placement of filaments showed superior results for cell growth. Staggered arrangement of filaments inhibit the cells falling straight to the bottom of the scaffold, which is facilitated by aligned stacking of filaments [43]. Yeo et al. [43] reported that changing the relative position of the filaments produces different pore sizes, which results in scaffolds more suitable for bone tissue regeneration. Afshar et al. [44] fabricated porous scaffolds using stereolithography based on triply periodic minimal surface, and characterised the mechanical properties by laboratory and computational experiments. Too et al. [45]

studied the strength of woodpile structures fabricated using FDM and observed a rapid reduction in strength when porosity is increased. Serra et al. [46] studied the role of microstructure on the mechanical properties and cell response therein, for various woodpile arrangements. Wu et al. [47] experimentally characterised the strength as a function of filament orientation in woodpile lattices of PEEK fabricated using FDM method. Martinez-Vazquez et al. [48] performed four-point bending of ceramic scaffolds and FE simulations to study the maximum stress within the filaments. In all these experimental, computational and theoretical studies, there appears to be no attempt to systematically bring out the *apparent modulus vs. porosity* relationship, despite their continued use in a range of practical contexts.

The review of the existing literature suggests that there is very little work on the modulus-porosity relationship for staggered woodpile lattices, when they are compressed in the stacking direction. The present work is inspired by this need. Here we consider the *compression* of such lattices in the stacking direction and present a simple analytical solution for apparent Young's modulus that can be associated primarily with *filament bending*. This simple theory is then refined by accounting for *filament shear*, which is more suitable for dense lattices. These very different mechanisms of filament deformation lead to completely different power law dependence of the apparent modulus with the porosity, as reported here. Besides, the possibility of stacking the alternate layers of filaments that are supported asymmetrically leads to the prospect of tailoring the stiffness by a significant factor, which depends on an asymmetry parameter α, as introduced here. The analysis of such lattices requires considering a periodically-supported, periodically-loaded elastic filament. The subsequent sections are arranged as follows. In Section 2, analytical models for the two arrangements are developed: first when the woodpile architecture is staggered in one direction, and second when it is staggered in both directions perpendicular to the direction of stacking. An analytical expression for apparent Young's modulus of asymmetrical arrangement in terms of skewness parameter α is also presented in this section. Predictions for the apparent stiffness are compared with FE simulations as well as experimental results on FDM 3D-printed specimens for a range of relative density are presented in Section 3. Discussions, including limitations of the high porosity limit formula, followed by scaling arguments, are provided in Section 4. Finally, conclusions are presented in Section 5.

2. Compressive stiffness of staggered woodpile lattices

The lattice structure, analysed here under compression, is shown in figure 1. The filaments (or struts) run parallel within a layer, but they are orthogonal across adjacent layers. The filaments within alternate layers do not overlap looking in the z-direction, therefore, we will refer to the configuration as *staggered* (see figure 1). An *aligned* arrangement of filaments with alternating layers has been studied elsewhere [38, 39]. When lattices in either staggered or aligned arrangements are remotely loaded along the x-axis or the y-axis, the elastic response is given by the elongation or compression of the filaments parallel to the loading direction. For a given volume fraction $\bar{\rho} = \pi r/2\lambda$, the apparent Young's modulus is identical for both arrangements along either x-, or y-directions, and is given by the rule of mixture [13, 30]. Here r is the radius of the

filament and λ is their lateral spacing. While the apparent Young's modulus along the *stacking direction* of the *aligned* arrangement has been previously studied [38, 39], the response of staggered lattices when compressed in the z-direction as shown in figure 1a has not been studied before. When the filaments are stacked in a staggered manner, the response is dominated by filament bending; whereas when the stacking is aligned, *diametrical compression* of the filaments is the main mechanism of deformation. Here, the stiffness in diametrical compression is assumed to be much greater than the flexural stiffness of the filaments, hence the flexibility of the supporting filaments is ignored throughout.

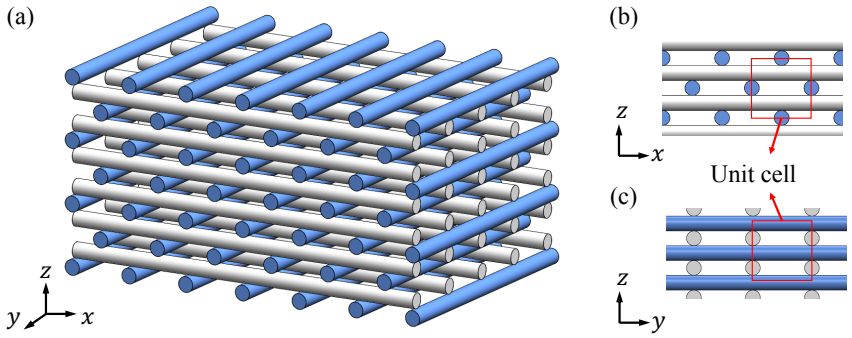

Figure 1: (a) Schematic diagram of the staggered woodpile arrangement.(b) Front view of the structure in the $x-z$ plane; blue shaded filaments are staggered in alternating layers, (c) side view of the structure in the $y-z$ plane; gray filaments in alternate layers are aligned.

2.1. Symmetrical unidirectional *stacking*

A unit cell within the elastic lattice is shown in figure 2a. Filaments within a layer act as supports for those in the layer above. Filaments propped this way, in turn, are loaded centrally by filaments in a layer above that are staggered relative to the filaments in a layer below (figure 1b). Under a compressive remote stress σ_∞ in the z-direction, the filaments that are parallel to the x-axis bend because of the constraints imposed by the filaments that are parallel to the y-axis. Filaments parallel to the y-axis do not bend. The diametrical compression is ignored in *all* struts. The bending of the four half-cylinders that appear parallel to the x-axis in figure 2a is shown in figure 2b. Because of the periodicity and the symmetry of the structure, the filaments can be treated as fixed-fixed beams under a transverse force F acting at the mid-point of its span λ (see figure 2c). The maximum transverse displacement, under the force F, is given by $\delta = F\lambda^3/192EI$, where E the Young's modulus and I the second moment of area of the filament cross-section.

The unit cell in figure 2b consists of a filament of diameter $2r$ at the centre, one above and one below, in addition to two halves—one at the top one at the bottom, adding up to a length $8r$ in the z-direction. The apparent compressive strain in the loading direction is given by the ratio $\langle\varepsilon\rangle = 2\delta/8r$. The number of squares of size $\lambda\times\lambda$

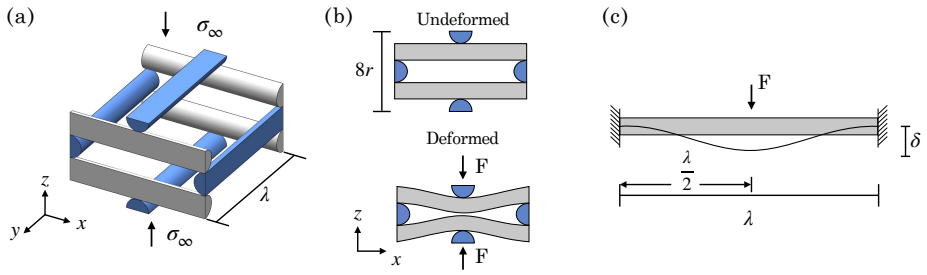

Figure 2: (a) An oblique drawing of the unit cell of a periodic woodpile lattice, (b) schematic diagram of an undeformed and a deformed unit cell—view along the y-direction, and (c) fixed-fixed beam model for a filament within a *symmetrically staggered* lattice. Supporting filaments running across are assumed to be stiff.

over which the force spreads, is half the number of filament pieces of length λ within a square grid, as N^2 squares are associates with $2N^2$ segments of length λ. Alternatively, each edge of length λ within a square grid contributes to two adjacent squares and since there are four edges per square, there must be twice the number of edges than the number of square. Combine this with the woodpile geometry that is exposed to loading over filaments that run *within each layer*, i.e. only one of the two orthogonal directions, the number of segments of length λ equals the number of $\lambda \times \lambda$ squares. Hence, the remote stress is given by $\sigma_\infty = F/\lambda^2$. Apparent quantities and properties will be indicated by angular brackets. Making use of the relationship $\langle E \rangle = \sigma_\infty / \langle \varepsilon \rangle$, the apparent Young's modulus is given by

$$\langle E \rangle_1 = (768 E I r)/\lambda^5. \tag{1}$$

The subscript 1 after the angular bracket reminds us that the lattice is unidirectionally staggered. Substituting $I = \pi r^4/4$ into (1), we have $\langle E \rangle_1 = 192 E r^5/\lambda^5$, i.e. $\langle E \rangle_1 \sim (r/\lambda)^5$. The apparent Young's modulus can be expressed as function of the volume fraction $\bar{\rho} = \pi r/2\lambda$ as

$$\langle E \rangle_1 = C E (\bar{\rho})^5, \tag{2}$$

where $C = 6144/\pi^4 \approx 63.07$ is a non-dimensional constant. The expression in equation (2) is valid for lattices with low relative density, as it is based on filaments modelled as slender beams in transverse deflection.

We further extend the applicability of equation (2) by taking into account the shear deformation in the bent filaments, when the spacing is small. Using Timoshenko correction, the traverse displacement of a beam shown in figure 2c is given by $\delta = (F\lambda^3)/(192EI) + (F\lambda/8S)$ [49], where S is the shear stiffness of filaments given by $S = \kappa G A_f$. Here G is the shear modulus of the material, κ is the shear correction factor, and A_f is the cross-sectional area of the filament. The expression for the apparent Young's modulus is thus refined as,

$$\langle E \rangle_{1-\mathrm{T}} = \frac{C E (\bar{\rho})^5}{1 + 48\pi^{-2}\kappa^{-1}(1+\nu)(\bar{\rho})^2}. \tag{3}$$

The subscript T refers to the apparent modulus when Timoshenko shear correction is included in filament bending. For materials with large porosity, i.e. $\bar{\rho} \ll 1$, the two expressions coincide. This confirms that, for low relative densities i.e. high porosity, Euler-Bernoulli micromechanics are adequate to predict the apparent Young's modulus of the lattice material. Taking $\nu = 0.36$ for PLA [50], and shear coefficient for circular cross-sections $\kappa = 0.9$ [51], we have

$$\langle E\rangle_{1-\mathrm{T}} \approx \langle E\rangle_1 \left[1 - 7.35\,(\bar{\rho})^2\right] + \mathrm{O}\left((\bar{\rho})^4\right). \tag{4}$$

For $r/\lambda = 1/10$, $\bar{\rho} = \pi/20$, which gives $\langle E\rangle_{1-\mathrm{T}} \approx 0.82\langle E\rangle_1$, indicating a correction of 18% for lattices with $\bar{\rho} < 0.15$. By contrast, doubling the spacing with respect to the filament diameter, i.e. for $r/\lambda = 1/20$, we get a correction of 4.53%; i.e. doubling the porosity approximately quarters the correction, which is consistent with the quadratic scaling in the correction term $7.35\,(\bar{\rho})^2$ above.

Analysis for lattices with staggered filaments in both x- and y-axes is taken up next. The alternate layers are still staggered symmetrically, i.e. the layer above is positioned in manner that λ-long struts are loaded centrally.

2.2. *Symmetric* bidirectional *staggered stacking*

Consider the lattice arrangement shown in figure 3. Filaments can be seen to be staggered across alternate layers in both x- and y-direction. Under the action of a remote stress σ_∞ in the z-direction, all the filaments in the lattice arrangement respond in bending, as opposed to the configuration analysed in the previous sections. A repetitive unit is shown in figure 3b. An analysis on the lines of that from equations (1) and (2) results in the expression for the apparent Young's modulus $\langle E\rangle_2 = (384EIr)/\lambda^5$, where the subscript 2 refers to the bidirectional arrangement. Comparing this with equation (1), we note that the bidirectionally staggered structure is softer by a factor of two. Therefore, the apparent modulus related to the apparent volume fraction as per

$$\langle E\rangle_2 = \frac{1}{2} CE\,(\bar{\rho})^5\,. \tag{5}$$

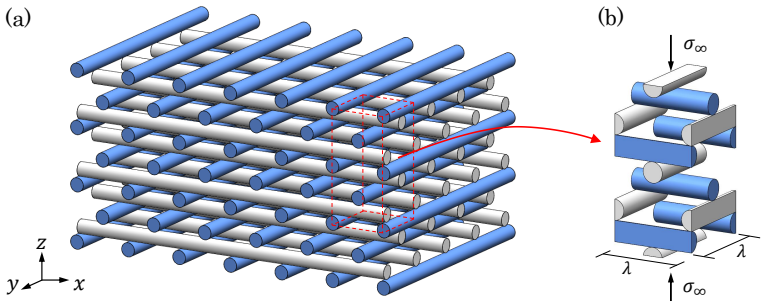

Figure 3: (a) Schematic sketch of the *doubly staggered* woodpile structure, (b) a repeating unit of the structure.

Models presented in Sections 2.1 and 2.2 are restricted to symmetrical staggered configurations, where the filaments lie at the midpoint of the overhang between the supports. The possibility of designing architectures with bespoke stiffness by positioning the staggered layers at an arbitrary offset affords interesting design opportunities to tailor the apparent stiffness. This general case is considered next.

2.3. Asymmetric *unidirectional arrangement*

Consider the lattice geometry shown in figure 4a, where filaments supported over two orthogonally placed filament are asymmetrically loaded. The elastic response of this lattice under a remote stress σ_∞ is expected to be primarily due to the bending of the filaments; all other deformations including shear and diametrical compression of filaments are ignored. A filament with periodic support and symmetric staggered arrangement (either unidirectional, or bidirectional), as discussed in the previous sections, has zero displacement and slope at the two ends —thus equivalent to fixed-fixed end conditions for a repetitive unit. For periodically supported filaments in asymmetric lattice (figure 4b), the zero deflection condition continues to be valid, provided the flexibility of the support filaments diametrically is ignored, which is a fair assumption for filament bending dominated well spaced lattices. However, *the zero slope condition is not applicable now*, which turns the analysis a little more involved. Therefore, the textbook case of *asymmetrically loaded beam of finite length* λ, with either fixed or supported conditions, is different from the *periodically-supported, periodically-loaded* problem considered here. So we now need a new analysis, accounting for appropriate translational symmetry present within infinite lattices.

Except at the point of loading and supports that we consider as rigid, filaments are free of external loading. So their deflection can be calculated by splitting the domain of analysis into two parts (figure 4c). The left side is modelled as a beam and has a length of $\alpha\lambda$, while the length of the remaining right side is $(1-\alpha)\lambda$. Here α serves as the skewness parameter, $0 < \alpha < 1$.

We define a coordinate system with origin at $\zeta = 0$ to be at the left support of the left part of the span, so that the transverse load is applied at $\zeta = \alpha\lambda$. For the right portion of the span, the load is applied at $\xi = 0$, the origin of the second coordinate system, so that the support at the right end is at $\xi = (1-\alpha)\lambda$. The displacements for the left and right beams, described by the variables $w_1(\zeta)$ and $w_2(\xi)$ respectively, are governed by the following two fourth order differential equations that are valid in the two different spatial domains

$$EIw_{1,\zeta\zeta\zeta\zeta} = 0,\ 0 \le \zeta \le \alpha\lambda; \quad \text{and} \quad EIw_{2,\xi\xi\xi\xi} = 0,\ 0 \le \xi \le (1-\alpha)\lambda. \tag{6}$$

Here each subscript after a comma represents differentiation with respect to that variable. As there is no external force between the supports and the location of loading, the right side of the above two equations is zero. The solution of the fourth order homogeneous differential equations immediate and is given by the two cubic expressions in the terms of the local coordinates ζ and ξ:

$$w_1(\zeta) = a_0 + a_1\zeta + a_2\zeta^2 + a_3\zeta^3, \quad \text{and} \quad w_2(\xi) = b_0 + b_1\xi + b_2\xi^2 + b_3\xi^3. \tag{7}$$

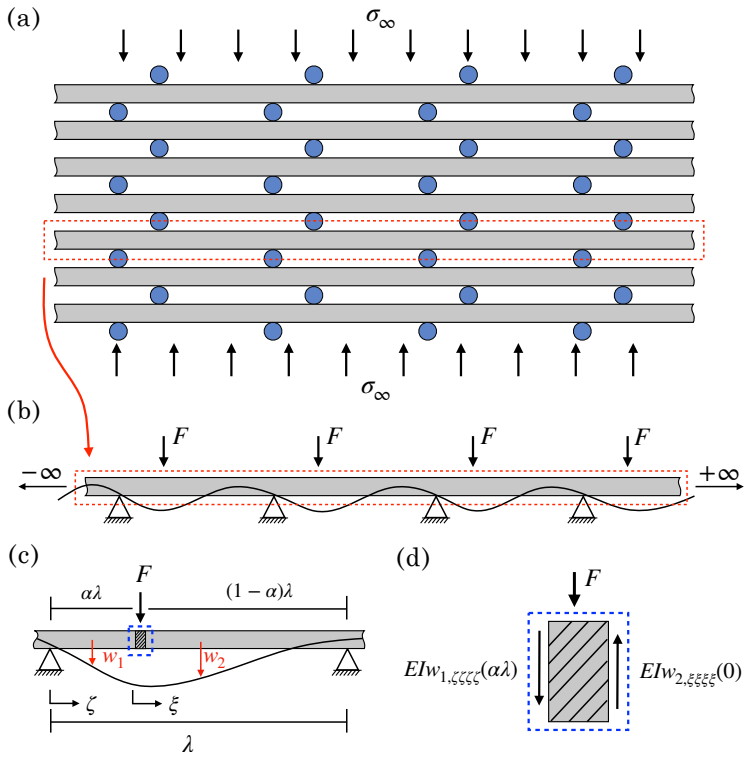

Figure 4: (a) Schematic diagram of the periodically-loaded, periodically-supported *asymmetric* staggered arrangement, (b) a single filament loaded and supported periodically, (c) a repetitive unit with asymmetrically placed point force, (d) Free body diagram of an infinitesimal element showing the shear force continuity at the point where the force F is applied.

These two solutions contain eight unknown constants a_0 to a_3 and b_0 to b_3. So we require eight boundary or periodicity conditions, accordingly. Note that the slope at the supports is not zero any more. Also, filaments at the supports are not curvature-free either, despite them being free from *external moment*. Kinematically consistent conditions at the supports, therefore, require invoking periodicity.

Firstly, displacement at the supports must be zero i.e. (i) $w_1(0) = 0$ and (ii) $w_2((1-\alpha)\lambda) = 0$. Due to the periodicity, there is slope continuity at the supports. Therefore, the slope $\partial w_1/\partial\zeta$ coming from the left $\zeta = 0^-$ must be equal to the slope $\partial w_1/\partial\zeta$ approaching from the right $\zeta = 0^+$. Because of translational symmetry, the slope and the moment at the left support $\zeta = 0$ must be equal those at the right support $\xi = (1-\alpha)\lambda$. The same argument holds for the curvature continuity, so that (iii) $w_{1,\zeta}(0) = w_{2,\xi}((1-\alpha)\lambda)$, and (iv) $w_{1,\zeta\zeta}(0) = w_{2,\xi\xi}((1-\alpha)\lambda)$.

Substituting these four boundary conditions into the solutions (7), we obtain a set of four *linear* algebraic equations. We require four further conditions to close the problem, as taken up next.

The continuity of displacement, slope, moment and the shear force at the point of application of the force F needs asserting. Displacement, slope and curvatures continuity are expressed respectively by the following three equations (v) $w_1(\alpha\lambda) = w_2(0)$, (vi) $w_{1,\zeta}(\alpha\lambda) = w_{2,\xi}(0)$, and (vii) $w_{1,\zeta\zeta}(a) = w_{2,\xi\xi}(0)$. The last of these is equivalent to moment continuity, but the term EI cancels out as there is no jump in the cross-sectional properties across the point of application of the force F. Finally, continuity of the shear force is imposed by considering a free body diagram of infinitesimal length along the beam centred at the point of application of F as shown in figure 4d, which results in (viii) $EIw_{1,\zeta\zeta\zeta}(\alpha\lambda) = EIw_{2,\xi\xi\xi}(0) + F$. Note that the derivatives in the above expression are with respect to the local coordinates ζ or ξ as appropriate. Substituting the four conditions within (v), (vi), (vii), (viii) into (7), we obtain four further algebraic equations that are linear in the eight unknowns.

Thus we have eight linear equations for the eight unknowns $a_0, ..., a_3$ and $b_0, ..., b_3$, arranged in the matrix form $\mathbf{Kq} = \mathbf{f}$, where $\mathbf{q} = \{a_0, \cdots, a_3, b_0, \cdots, b_3\}^T$, $\mathbf{f} = \{0, 0, 0, 0, 0, 0, 0, F/(6EI)\}^T$. The coefficient matrix in the above set of equations is given in Appendix equation (A1). The eight simultaneous equations can fortunately be obtained by manually solving eight simultaneous linear equations, consistent with that from symbolic algebra using Mathematica® used as a check (the final solution for eight unknown are given in appendix equations (A2a)-(A2h)), which results in the final profile of the span given by

$$w_1 = \frac{F}{12EI}[(\alpha - \alpha^2)(2\alpha - 1)\lambda^2\zeta - 3\alpha(1-\alpha)\lambda\zeta^2 + 2(1-\alpha)\zeta^3], \quad 0 < \zeta \leq \alpha\lambda, \tag{8a}$$

$$w_2 = -\frac{F}{12EI}[\alpha^2(1-\alpha)^2\lambda^3 - (\alpha - \alpha^2)(2\alpha - 1)\lambda^2\zeta - 3(\alpha - \alpha^2)\lambda\zeta^2 + 2\alpha\zeta^3], \quad \alpha\lambda < \zeta \leq \lambda. \tag{8b}$$

Compare these with the expressions for profiles, obtained using kinematically inconsistent support conditions, that are presented in the Appendix equations (A4) and (A3). Profiles of the deflected shape between two consecutive support points are shown in figure 5. In all these sub-figures, the point of application of force from filaments above are indicated by a red dot. Figure 5a shows profiles for periodically-supported periodically-loaded filament along with results from clamped and simply supported finite-length beams for $\alpha = 0.8$ (see equations (A4) and (A4)). Simple support grossly over-estimates deflections (exactly by a factor of 4 under the load), whereas clamped supports under-estimates it. The effect of the location of loading, as dictated by the skewness parameter α is brought out by figure 5b. Similar trends for clamped and simply supported finite beams are presented in figures 5c and 5d. Clamped conditions, although incorrect, provide a reasonable estimate for deflection under periodic load, especially for slight asymmetry (i.e. $\alpha \approx 0.5$), unlike simple support.

The deflection δ under the force F, arising from interaction with filaments above and below running across, is given by

$$\delta = \left(\frac{F\lambda^3}{3EI}\right) \times \frac{\alpha^2(1-\alpha)^2}{4}. \tag{9}$$

Compare the above expression for the deflection under a periodically supported peri-

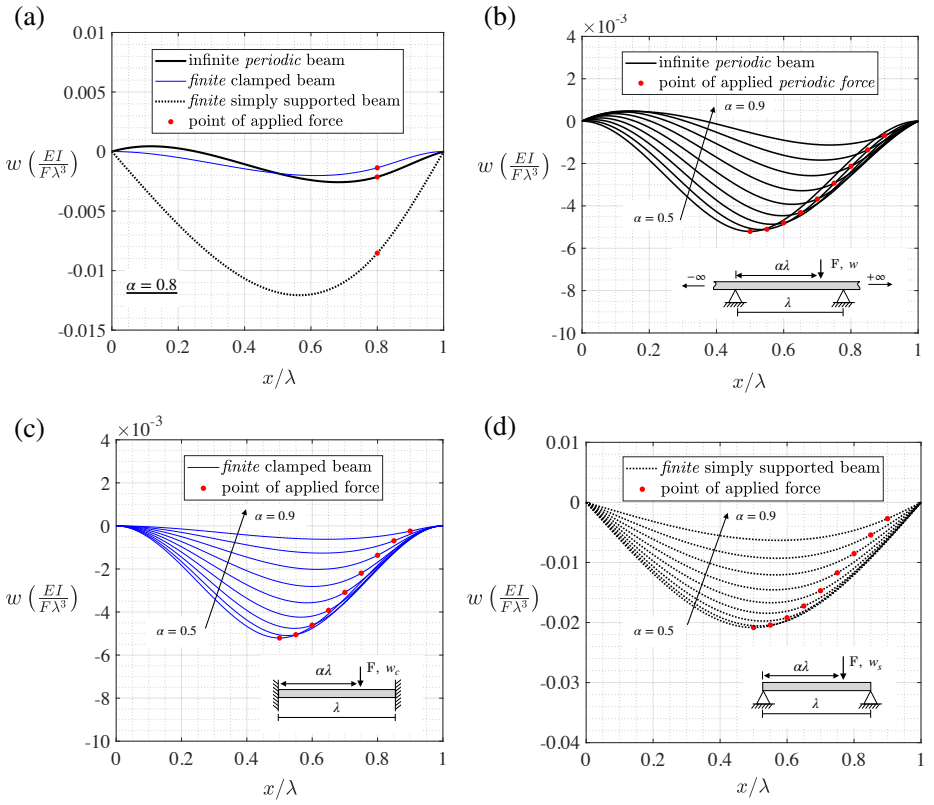

Figure 5: Non-dimensional displacement profiles. (a) comparisons between infinite periodic beam, finite clamped, and finite simply supported beam for α=0.8, (b) infinite periodic beam for range of values of α, (c) finite clamped beam for a range of values of α, and (d) finite simply supported beam for a range of values of α. Red dots on each plot shows the point of application of load.

odically loaded beam with those for an asymmetrically loaded finite beam

$$\delta' = \left(\frac{F\lambda^3}{3EI}\right) \times \alpha^3(1-\alpha)^3, \tag{10a}$$

$$\delta'' = \left(\frac{F\lambda^3}{3EI}\right) \times \alpha^2(1-\alpha)^2 = 4 \times \delta, \tag{10b}$$

where δ' and δ'' refer to the deflection under asymmetrically placed load on a clamped and simply supported beams, respectively. Clearly δ'' is always incorrect by a factor of 4, but its functional dependence with the skewness parameter α is the same as that of the periodic beam solution δ, whereas the finite beam expression δ' has a different functional dependence on α and it always underestimates the deflection, except for $\alpha = 0.5$ when $\delta = \delta'$.

The two extreme cases of simplification (i.e. a span of fixed length λ that is either simply supported, or clamped at both ends) provide upper and lower bounds of the

estimates of the lattice deflection in compression, $\delta' < \delta < \delta''$.

Displacement at the point of the application of F, $\delta = w_1(\alpha\lambda) = w_2(0)$, enables us to calculate the apparent lattice strain. The apparent Young's modulus of the lattice material in compression along the stacking direction $\langle E\rangle_{1,\text{Asym}}$ can then be calculated using the apparent strain and the remote stress. Substituting equation (9) into $\langle\varepsilon\rangle = 2\delta/8r$ and $\langle E\rangle = \sigma_\infty/\langle\varepsilon\rangle$, the expression for the apparent Young's modulus is obtained as

$$\langle E\rangle_{1,\text{Asym}} = \frac{48EIr}{\alpha^2(1-\alpha)^2\lambda^5}, \quad \text{where} \quad 0 < \alpha < 1. \tag{11}$$

The denominator in the above equation vanishes if $\alpha = 0$ or $\alpha = 1$ implying high stiffness if the filaments are close to becoming aligned in the stacking direction. Equation (11) can be further simplified by separating the volume fraction dependence of the apparent stiffness from the dependence upon the *skewness parameter* α, which can be captured by a function $\phi(\alpha)$. Thus the expression for the apparent modulus takes the following form:

$$\langle E\rangle_{1,\text{Asym}} = CE(\bar{\rho})^5\phi(\alpha), \text{ where } \quad \phi(\alpha) = \frac{1}{16}(\alpha)^{-2}(1-\alpha)^{-2}. \tag{12}$$

The expression for $\phi(\alpha)$ contains the dependence of $\langle E\rangle_{1,Asym}$ on the relative position of the filaments via the non-dimensional geometric parameter α, which is plotted in figure 6. As $\alpha < 1$, $\phi(\alpha)$ is always greater than 1, which means asymmetry within staggered woodpile lattices increases stiffness i.e. $\langle E\rangle_{1,\text{Asym}} > \langle E\rangle_1$, for the same level of porosity. The variation of ϕ in the interval $0.3 < \alpha < 0.7$ is fairly gentle. When this parameter is close to 0 or 1, representing a very asymmetric placement of the alternating layers, $\phi(\alpha)$ increases steeply. For symmetrically staggered filaments, $\alpha = 0.5$, for which $\phi(0.5) = 1$, so that equations (11) and (12) coincide with equations (1) and (2), respectively. This is further taken up in Section 3.1, where the importance of the correct slope continuity at the supports is brought out with FE simulations. Equation (10b) refers to an asymmetrical force F applied on a simply supported finite beam is also plotted with dotted line in figure 6. Stiffness obtained from this is incorrect by a factor of four for all values of α.

The increment in stiffness is caused by the reduction in length on one sides of the filament, increasing its resistance to bend. The model developed here is limited to positions in which the parameter α is such that it still gives enough length for the filament to bend. When α approaches 0 or 1, the prediction of $\langle E\rangle$ becomes far more complex, because the diametrical compression becomes a significant part of the total lattice compression. We do not cover this extreme case here. But, in the limit of $\alpha = 1$, the equation (11) becomes singular.

3. Departure from high porosity asymptotic behaviour: computations and measurements

Analytical expressions for the apparent lattice stiffness derived in the previous section are now reconciled against FE calculations using the commercial code Abaqus/CAE/Standard 6.13® (Simulia, Dassault Systemes, Providence, RI, USA)

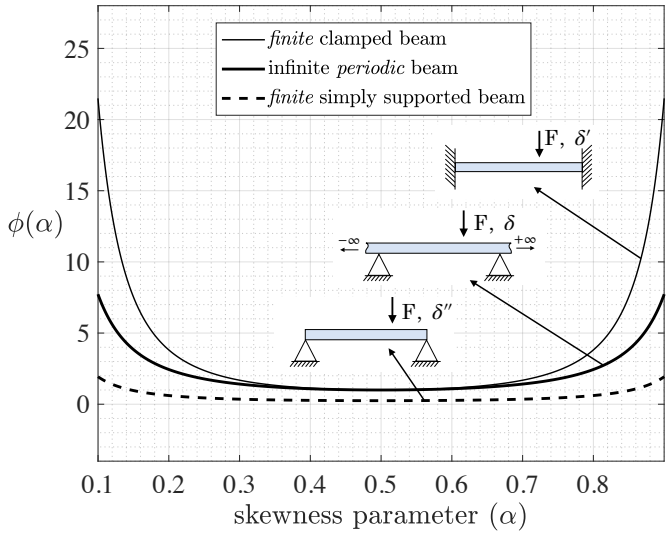

Figure 6: The function $\phi(\alpha)$, when kinematically consistent *periodic boundary conditions* are used (solid line), and when an approximation of finite length clamped and simply-supported is used (thinner, and dotted lines, respectively).

[52]. Filaments that constitute the lattice were modelled as elastic cylinders and meshed using ten-noded tetrahedral C3D10 solid elements that use quadratic interpolation. Bonding between the filaments was modelled using a small overlap in the volume of the adjacent cylinders (4% of radius). The radius of the cylinders was taken as $r = 0.25,\ 0.3,$ and 0.4 mm (this choice is based on the size for the available nozzles for FDM 3D-printers in the market). The rest of the geometric parameters such as the separation between the filaments λ, were changed systematically to study their influence on the apparent elastic modulus. By varying r and λ systematically, porous lattices of varying relative density $\bar{\rho}$ were simulated. The material properties for PLA are taken from the literature, i.e. $E = 2290$ MPa (data measured from tensile tests on single FDM-filaments [53]), and the Poisson's ratio $\nu = 0.36$ [50].

3.1. Symmetrically *staggered lattices: computations*

We modeled repetitive units of unidirectionally and bidirectionally lattices that are staggered symmetrically. Analysis of unit cells with appropriate translational symmetry conditions provide computational economy. Various unit cells, such as those shown in figure 7a for unidirectional and figure 7b for bidirectional lattices, were subjected to compressive forces within FE simulation. In each simulation, a rigid plate was tied to the nodes at the top surface. A uniform compressive pressure was applied to this plate at the top. The nodes on the bottom surface were constrained in all degrees of freedom, while due to periodicity of the structure, all the nodes lying on the vertical surfaces were constrained to remain in their plane, allowing displacements within those planes.

The deformed shape and von Mises stress distribution under a constant compressive strain in z-direction for symmetrically unidirectional and bidirectional staggered lattice structure as obtained from the FE simulations are presented in figure 7. Note the predominantly bending deformation of the filaments in bidirectionally staggered lattice, whereas for the unidirectionally staggered structure, only filaments running parallel to the y-direction contribute to the deformation of the unit cell. The von Mises stresses for unidirectionally staggered lattice are higher than those for the bidirectionally staggered structure for the same level of remote stress, which indicate the unidirectional staggered is stiffer that bidirectional staggered and is consistence with equations (2) and (5).

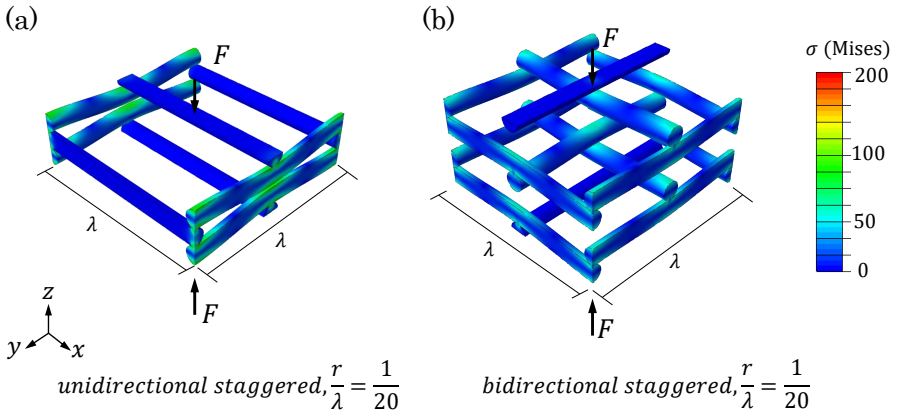

Figure 7: Deformed shapes and von Mises stress distributions within a repeating unit under constant compressive strain obtained from the computational experiments on (a) unidirectionally staggered lattice (b) bidirectionally staggered lattice. The deformed shapes have been scaled up for better visualization.

The apparent Young's modulus was calculated by spreading the force over the projected area and accounting for the different lengths in the z-direction for the two lattice configuration. The apparent Young's modulus calculated from simulations is plotted as a function of the relative density in figure 8. The values for unidirectional staggered arrangement are presented using square markers. The trend is above that for the bidirectional staggered arrangement shown using circles by a constant factor, which reflects a constant separation between the two trends on a log-log graph. The apparent Young's modulus scales $\langle E \rangle \sim (\bar{\rho})^5$ for both arrangements, as predicted by our analysis (see, equations (2) and (5)). Theoretical straight lines with slope 5 on a log-log plot in figure 8 confirm this. The apparent Young's modulus obtained with shear correction does not follow a simple power law (see equations (3) and (4)). The same is true of FE simulations that show a slight departure from the fifth power law as a falling slope on the log-log plot is observed. When the tangent for low relative density is drawn to FE data, they correspond to $\langle E \rangle \sim (\bar{\rho})^{4.8}$ for unidirectional staggered, and according to $\langle E \rangle \sim (\bar{\rho})^{4.7}$ for doubly staggered lattices, in the asymptotic limit of high porosity (figure 8). As $\bar{\rho}$ increases, the ratio r/λ increases resulting in short and thick filaments, where the beam theories are not applicable. Inclusion of shear significantly improves

the agreement between numerically obtained results and analysis.

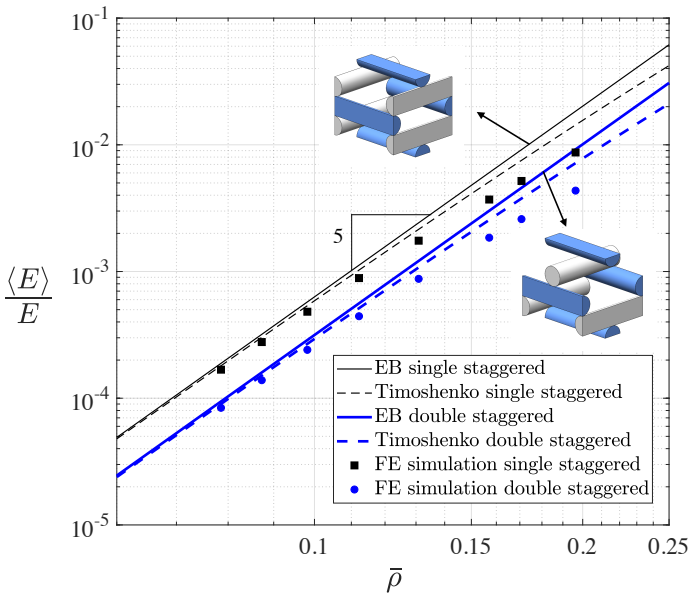

Figure 8: Comparison of modulus vs porosity as predicted using analyses and the FE simulations. Results obtained using Euler-Bernoulli (solid lines) and Timoshenko (broken lines) models for the filament flexure are presented for unidirectional (thin-black) and bidirectional (thick-blue) staggered arrangements.

3.2. Asymmetrically *staggered lattices: computations*

We carry out FE simulations of a periodically supported periodically loaded beams for different skewness parameter α. The complete displacement profile of an asymmetrically loaded, periodically supported, filament is shown in figure 9 compared with the theoretical analysis obtained in equation (12). The geometric properties are: overhang $\lambda = 6$ mm, cross-sectional radius $r = 0.3$, and it is subjected to periodic comb of point force of magnitude $F = 1$ N for $\alpha = 0.8$. Due to shear, the deflection profile obtained from FE is slightly different from theoretical solution.

Woodpile structures in figure 10 show the deflection profile, obtained from FE simulations, when the lattice structure is subjected to compressive loading. Von Mises stress distribution of symmetrical a asymmetrical staggered arrangements are compared for a similar in-plain compressive strain. The filament radius is $r = 0.3$ mm. The overhang between filaments is equal to $\lambda = 6$ mm. Filaments do not lie at the midpoint of the overhang to produce asymmetric configuration, the degree of asymmetry being controlled by the parameter α. The deformed shape in figure 10 corresponds to $\alpha = 0.7$. The non-zero slope at the support filaments is observed in the inset of figure 10b; compare this with the inset of figure 10a for symmetrically staggered lattice that shows zero slope at the supports.

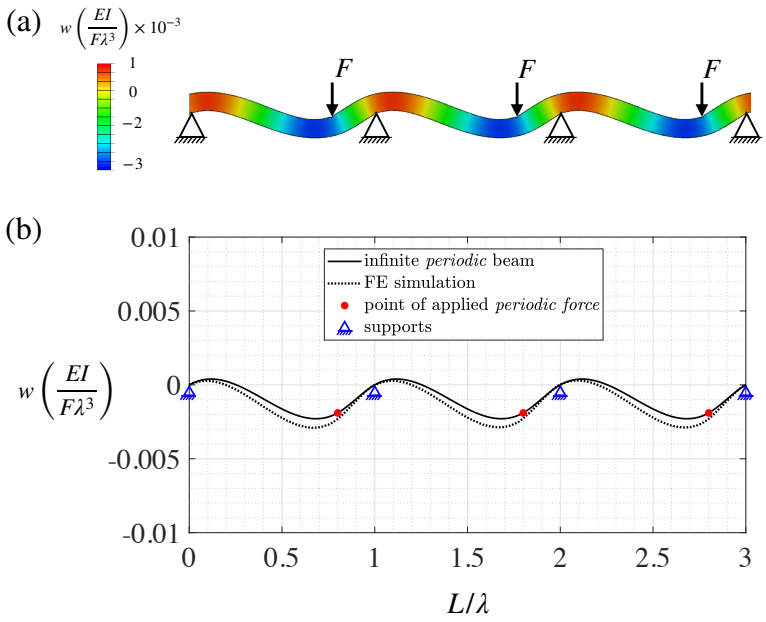

Figure 9: Comparison of deflection curves obtained from (a) FE simulations of periodically loaded beam and (b) theoretical models. Skewness parameter $\alpha = 0.8$.

The apparent Young's modulus obtained from the FE simulations for a finite lattice was compared against the predicted trends calculated using equation (12), as shown in figure 11. Results from FE calculations are compared with those from the analytical model consistent with periodic boundary conditions, along with those from pinned and clamped supports conditions that are inconsistent with the translational symmetry, yet they provide bounds via a simple analysis (figure 11). The top line corresponds to the apparent modulus obtained from an analysis of the filaments with zero slope at the supports. The bottom dotted line corresponds to results from an analysis with pinned supports at the ends. The solid line corresponds to the model based on the periodic beam, developed in Section 2.3. The agreement between the periodic beam model and the FE simulations is excellent, which validates the analysis. The dotted lines in figure 11 are the upper and the lower bounds for the apparent Young's modulus. The correct response lies between these two, and thus correctly predicted with the model developed in Section 2.3. The lowest value for $\langle E \rangle$ in figure 11 corresponds to the symmetric staggered configuration corresponding to $\alpha = 0.5$. As expected $\langle E \rangle$ increases as the ratio α approaches 1, where equation (11) has singularity at $\alpha = 1$. The periodic beam theory presented here has two omissions that are attributed to the difference between the FE computations and the analysis.

3.3. Fabrication of woodpile lattices and measurement of their apparent modulus

Following the analysis and computations presented in the previous sections, we carried out an experimental programme to establish the modulus-porosity relationship.

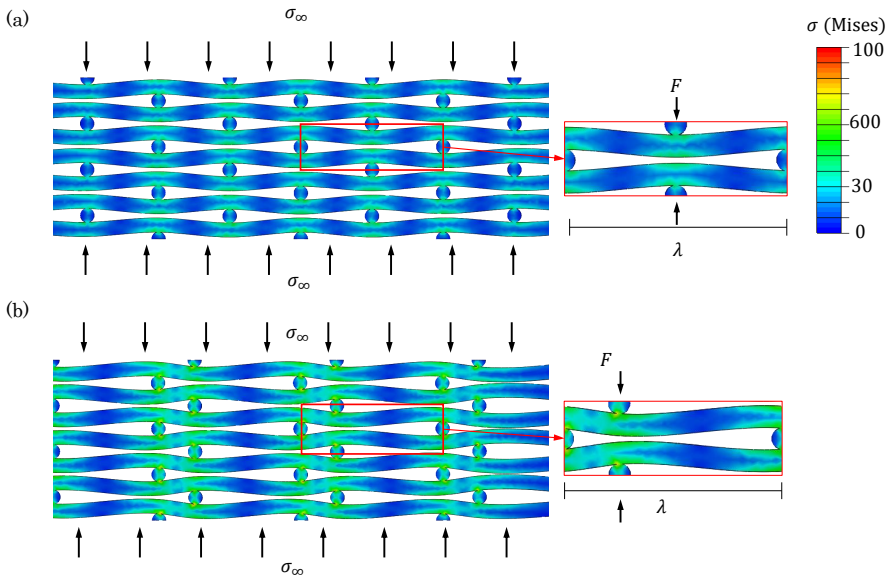

Figure 10: Deformed shapes obtained from FE calculations for (a) symmetrical and (b) asymmetrical arrangements. Both show the deflection of the filaments in primarily in flexure. Note the comparison in the insets between (a) and (b) that have zero and non-zero finite slopes, respectively.

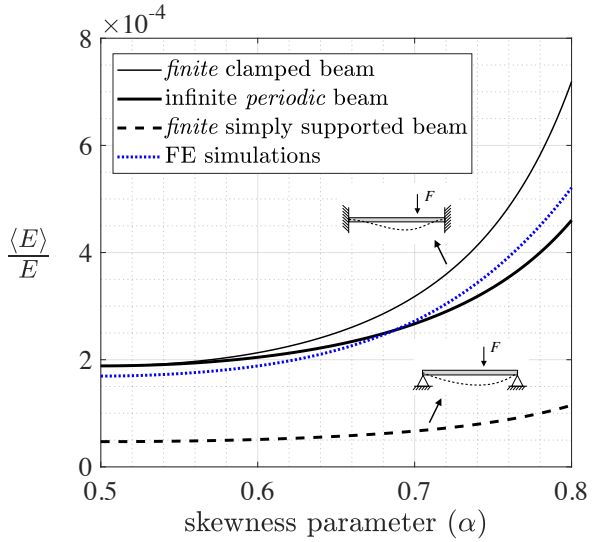

Figure 11: Relationship between the apparent Young's modulus and the relative position of the filaments in the staggered configuration.

Lattice structures with controlled spacing λ and varying nozzle diameter d were fabricated, which provided a range of porosity and enabled us to measure the apparent stiffness of such structures as a function of the volume fraction. Fused deposition modelling using polylactic acid (PLA) was employed for fabrication because of the affordability and control on the geometry of the process that it offers. Besides these, many practical structures such as those for tissue engineering are actually produced using this manufacturing process.

Woodpile lattices were fabricated by driving the print head by a bespoke G-code developed by us that allowed lattice spacing to be changed at will. Additionally, changeable nozzles were used to vary the filament diameter. Ultimaker^2 Extended+ 3D-printer was used to fabricate the test specimens. All specimens were fabricated at 205 °C with speed of 1000 mm/min and fan speed of 80%. Overlap between layers was set at 4% of the diameter for all specimens. SEM micrograph of cross-section of woodpile structures printed with 0.4 mm and 0.6 mm nozzle are shown in figure 12. There is a deviation of the diameter of the extruded filaments from the nominal nozzle diameter, which is less than 9%. As expected, there is flattening of the extrusion so that the diameter is slightly wider horizontally and slightly shorter vertically, resulting in ellipticity of a small degree. Our measurements for printed samples using 0.4 mm nozzles show horizontal and vertical diameter of the fabricated extrusions as (434 ± 7) μm and (380 ± 7) μm, respectively. These measurements for the 0.6 mm nominal diameter nozzles are (623 ± 8) μm and (587 ± 7) μm, respectively. The variance is due to inevitable variability in the fabrication process, whereas difference in the mean vertical dimensions vs that in the horizontal direction is due to flattening of the molten material during solidification, which is a systematic deviation from the intended structures. The relative density of specimens are calculated by using the total weight, the material density and the total external volume of the printed cubic samples. The length and width of cuboid test specimens were chosen according to the ASTM standard D1621 to be 50 mm $\times$ 50 mm and their height was approximately 25 mm. Instron 5569 testing machine was used to perform uniaxial compression tests with strain rate of 3×10^{-4} s^{-1}. Dino-lite microscope was used to capture images during the tests.

3.4. Experimental determination of modulus-porosity relationship

Two typical stress-strain curves obtained from experiments are presented in figure 13. The standard deviation is shown used the shaded band around the mean curves. The response is non-linear when the strain is finite. There are four stages of deformation that can be identified: (1) bending of filament segments supported by neighbouring rods, (2) yielding of these segments followed by non-linear response, (3) plastic deformation of these filaments under bending, (4) contact and densification of layers. These phases are shown in the figure using four key points, as labelled. The apparent Young's modulus was assessed by considering the linear response at the initial phase of the deformation. For each specimen, the apparent density was calculated by weighting sample before test and dividing by its volume based on its external shape and material density. Thus, from samples of different lattice spacing λ and filament diameter d, the relationship between the volume fraction and the apparent modulus can be experimentally determined.

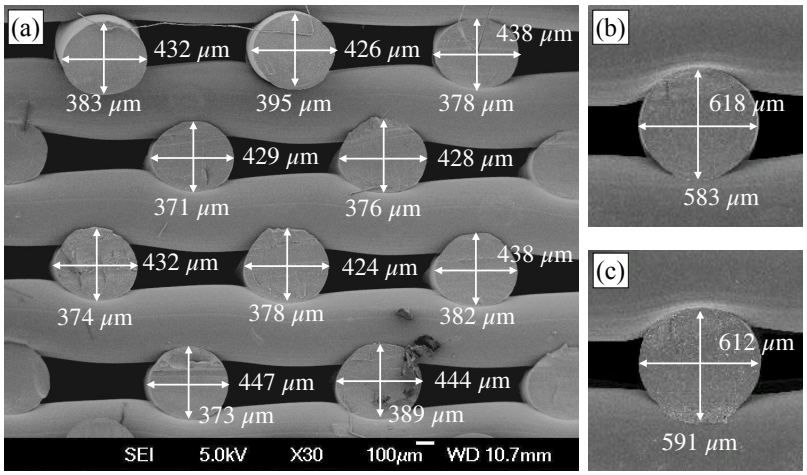

Figure 12: SEM micrograph of a FDM fabricated staggered woodpile structures with (a) 0.4 mm and (b)-(c) 0.6 mm nozzles. The measurements shows a deviation less than 9% of the diameter of the extruded filaments from the nominal nozzle diameter.

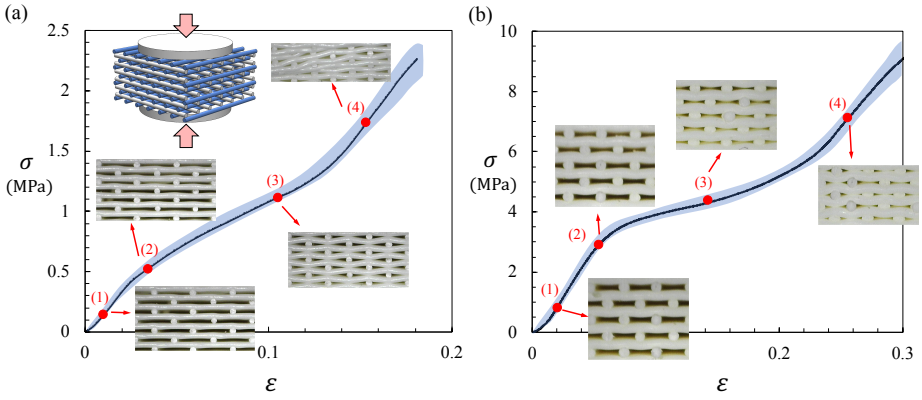

Figure 13: Average stress strain curve for 3D-printed samples under compression (a) nozzle diameter $d = 0.4$ mm; spacing 2.1 mm, and (b) $d = 0.6$ mm; spacing 1.6 mm. Accompanying images were acquired during the tests. The standard deviation is within the shaded area.

Figure 14 shows a comparison between theoretically predicted power law relationship, FE simulations, and the experimentally obtained measured modulus vs apparent density relationship. Experimental data for two different nozzle diameter are overlaid on to a single graph. For small values of apparent density, the results fall closely along a line of slope 5 on a log-log plot, as predicted by the analysis. Deviations from the theoretical asymptotic fifth-power law are observed for larger values of the apparent density. The experimental results diverge from the theoretical trend, showing an increasingly softening. However, the experimental data points (dots with experimental error bars) match well with FE calculations (dotted line). The difference between the measurements and FE simulations are potentially due to fabrication errors as well as measurement errors - both have a *random* character. On the other hand, the difference between the theoretical power law and the computations/measurements is *systematic* softening, and can be attributed to a number of simplifications in the analysis e.g. (i) ignoring shear in the filaments, (ii) diametrical compression being assumed to be negligible, (iii) unaccounted for 3D effects in super-dense lattices, (iv) a small degree of inevitable ellipticity of the profile of the extrusion—our models assume circular cross-section, by contrast.

It is often possible to carry out simple relationships using scaling arguments—often used by physicists very effectively (see for example, Gibson and Ashby [22], Warner & Edwards [29] in the context of solid foams). Unlike the well known cases of planar honeycombs and open cell 3D foams that show $\langle E\rangle \sim \rho^3$ and scaling respectively, our detailed analysis shows a fifth power law. This suggests that the existence of simple power law relations between the apparent modulus and the porosity for woodpile lattices, without the recourse to detailed analysis. Arguments in this spirit are presented in the following section.

4. Scaling arguments and discussions

Equation (12) highlights that the apparent modulus scales with porosity according to $\langle E\rangle \sim (\bar{\rho})^5$, for a fixed $\alpha\lambda$, i.e. a fixed asymmetry of stacking. This power law dependence of the apparent modulus upon porosity was also observed previously for symmetric stacking in one direction as well as both directions (equations (2) and (3), respectively).

Expressions from these specific analyses suggest that the underlying modulus-porosity scaling leading to equations (2), (5), and (12) may be much more general. The flexural stiffness of filaments scales according to EI/λ^3. The transverse deflections scales as $\delta \sim F\lambda^3/(Er^4)$. So, the apparent transverse strain in scales according to $\langle\epsilon\rangle \sim \delta/r$, so that $\langle\epsilon\rangle \sim F\lambda^3/(Er^5)$; transverse force scales as per $F \sim \sigma_\infty \times \lambda^2$. Combining this with $\overline{\rho} \sim (r/\lambda)$, we obtain a power law relating the apparent modulus of elasticity with the volume fraction as

$$\langle E\rangle \sim E\,(\overline{\rho})^5\,. \tag{13}$$

The constant of proportionality *cannot* be determined from scaling arguments alone and requires detailed analysis, computations, or experimentation.

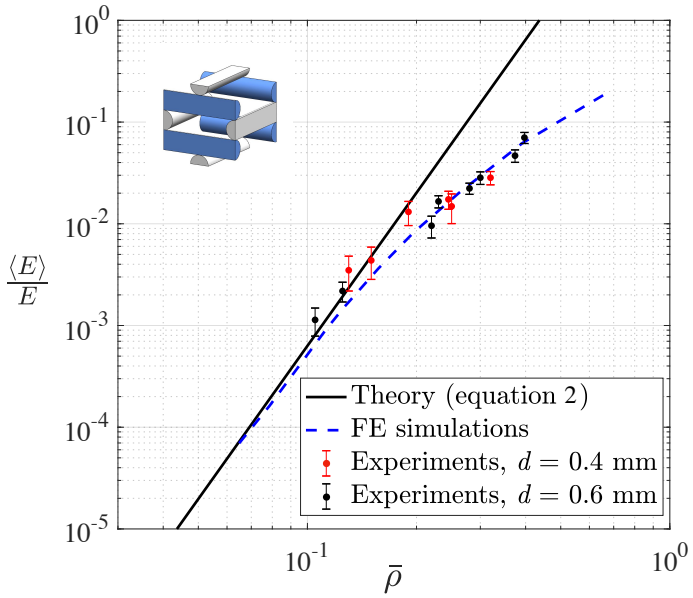

Figure 14: Comparison of the modulus-porosity relationships: (i) as predicted by analysis (solid line), (ii) with FE calculations (dotted line), and (iii) experimental results obtained from compression test of several 3D-printed samples (each marker refers to a sample of specified porosity), fabricated using different filament diameter and lattice spacing.

When alternate layers are staggered asymmetrically, displacement under the force, at a distance $a = \alpha\lambda$ from one end, can be expressed as $\delta = \delta(F, EI, \lambda, a)$, the problem having $n = 5$ parameters. Since EI appear together in bending mechanics, they are combined. Carrying out dimensional analysis [54], choosing "force-length-time" as the fundamental variables (instead of "mass-length-time"), the five dimensional variables can be expressed in terms of just $m = 2$ dimensions (force and length). Invoking Buckingham's Π-theorem [55, 56], the relationship between all the variables of the problem can be expressed in terms of $n - m = 3$ dimensionless groups. Choosing EI and λ as scales, with unknown exponents assigned to them, the remaining three dimensioned variables can, in turn, be multiplied to form the Π-groups. This results in the three non-dimensional numbers as $\Pi_1 = F\lambda^2/(EI) = F^*$, $\Pi_2 = \delta/\lambda = \delta^*$, and $\Pi_3 = a/\lambda = \alpha$. Thus the force-response relationship could then be written as

$$\delta^* = f\,(F^*, \alpha)\,. \tag{14}$$

Since we are interested only in small lattice strain to define the apparent modulus in a meaningful way, the proportionality $\delta \sim F$ must hold. For this to be true, the function f must factorise with a term involving F factored out. This means that the functional dependence $\delta \sim (F\lambda^3)/(Er^4) \times \phi\,(\alpha)$ must hold. Using arguments leading to equation (13), we obtain a general power law for the dependence of the apparent Young's modulus with the volume fraction

$$\langle E\rangle \sim E\,(\bar{\rho})^5\,\phi\,(\alpha)\,. \tag{15}$$

Neither the constant of proportionality in the above scaling relation, nor the functional form of ϕ can be determined without detailed analysis. Note that the function ϕ above is the same as that presented previously within equation (12), where its functional form was analytically derived.

The above scaling result is consistent with detailed analyses presented in the previous sections for various geometries—i.e. unidirectionally staggered symmetrical, bidirectionally staggered, or asymmetric lattices. The constants of proportionality for the three cases are $C = 63.07$, $C/2 = 31.54$, and $C\phi\,(\alpha) = 63.07 \times \phi(\alpha)$, respectively. Let us contrast the power law dependence observed here with other well known scaling laws in the mechanics of porous and cellular media. For hexagonal honeycombs, the power law is known to be cubic, i.e. $\langle E\rangle \sim E(\bar{\rho})^3$ [23]. For foams, this dependence is quadratic, i.e. $\langle E\rangle \sim E(\bar{\rho})^2$, indicating that the rate at which the transverse stiffness diminishes with increasing porosity is much more rapid than that for honeycombs and foams [24]. The constants of proportionality are quite different for each case, of course. The micro-mechanics in all these three cases, i.e. honeycombs, foams and woodpile lattice is bending-dominated; the difference in the power laws is attributed to the dimensionality and the differences in the architecture. Note that a power law scaling of the apparent properties is not always guaranteed —such simple scaling relationships, when they exist, are therefore of great practical interest due to their simplicity and ease of use.

5. Conclusions

The relationship between the apparent modulus of elasticity along the stacking direction, and the structural parameters of a lattice of elastic filaments in a woodpile form, is studied analytically, computationally, and experimentally. Symmetric as well as asymmetric staggered configurations are considered. Expressions for the apparent structure-property relationship are developed on the basis of the micro-mechanics of bending.

The dependence of the apparent Young's modulus on the extent of the staggered position of the filaments is brought out. This is described by an analytical function that shows largest flexibility of the lattice when it is symmetric. The expression for the apparent Young's modulus shows a scaling relation with the volume fraction given by $\langle E \rangle \sim (\bar{\rho})^5$, showing a very high sensitivity to volume fraction, unlike some other previously known modulus-porosity relationships. This simple expression is then modified to include correction due to shear in the filaments. The leading correction term shows reduction in the modulus for a given volume fraction, which is associated with filament shear. The asymmetrically staggered lattice is then analysed using a model of periodically-supported periodically-loaded filament. Expressions for the apparent modulus are obtained as a function of the porosity and a skewness parameter. Two simple expressions for the apparent modulus provide upper and the lower bounds. Results from the analytical models were developed as function results were validated against FE computations, showing excellent agreement.

Finally, woodpile structures of a range of porosity values were fabricated using 3D-printing. This was achieved by controlling the lattice spacing and the using different nozzles to produce filament of different diameter. Experimental characterisation of the lattice stiffness using compressive testing on several samples produced a power law trend of the apparent Young's modulus as a function of the porosity, which is found to be consistent with the theory presented here. For dense samples, the deviations from the power law are attributed to unaccounted for deformations e.g. filament shear and diametrical compression. The experimental modulus-porosity relationship agrees well with detailed FE simulation.

As a general conclusion, analytical expressions for the apparent stiffness along the stacking direction of the woodpile lattice material were provided for various arrangements of the woodpile. Excellent agreement with finite element calculations and experiments were found. The results are consistent with scaling arguments presented for a power law dependence between the apparent modulus and the relative density of the porous lattice.

Acknowledgements

Support to EC-U from the Mexican Science and Technology Council (CONACyT) and to FS by a Marie-Curie doctoral training network (HyMedPoly) are gratefully acknowledged.

References

[1] N. A. Fleck, V. S. Deshpande, M. F. Ashby, Micro-architectured materials: past, present and future, Proceedings of the Royal Society A: Mathematical, Physical and Engineering Sciences 466 (2121) (2010) 2495–2516.

[2] V. Dikshit, A. P. Nagalingam, Y. L. Yap, S. L. Sing, W. Y. Yeong, J. Wei, Crack monitoring and failure investigation on inkjet printed sandwich structures under quasi-static indentation test, Materials & Design 137 (2018) 140–151.

[3] R. Lakes, Materials with structural hierarchy, Nature 361 (6412) (1993) 511–515.

[4] D. W. Hutmacher, Scaffolds in tissue engineering bone and cartilage, Biomaterials 21 (24) (2000) 2529–2543.

[5] J. A. Lewis, Direct ink writing of 3d functional materials, Advanced Functional Materials 16 (17) (2006) 2193–2204.

[6] C. Paredes, F. J. Martinez-Vazquez, A. Pajares, P. Miranda, Novel strategy for toughening robocast bioceramic scaffolds using polymeric cores, Ceramics International 45 (15) (2019) 19572–19576.

[7] C. Paredes, F. J. Martínez-Vázquez, A. Pajares, P. Miranda, Development by robocasting and mechanical characterization of hybrid ha/pcl coaxial scaffolds for biomedical applications, Journal of the European Ceramic Society 39 (14) (2019) 4375–4383.

[8] Y. Liu, H. Wang, J. Ho, R. C. Ng, R. J. Ng, V. H. Hall-Chen, E. H. Koay, Z. Dong, H. Liu, C. W. Qiu, J. R. Greer, J. K. Yang, Structural color three-dimensional printing by shrinking photonic crystals, Nature Communications 10 (1) (2019) 1–8.

[9] A. R. Weily, K. P. Esselle, B. C. Sanders, T. S. Bird, A woodpile ebg sectoral horn antenna, in: 2005 IEEE Antennas and Propagation Society International Symposium, Vol. 4, IEEE, 2005, pp. 323–326.

[10] X. Lu, Y. Lee, S. Yang, Y. Hao, J. Evans, C. Parini, Extrusion freeforming of millimeter wave electromagnetic bandgap (ebg) structures, Rapid Prototyping Journal 15 (1) (2009) 42–51.

[11] Z. Feng, T. Fu, B. Yan, R. Liu, Investigation for ultra-shorten coupling length in woodpile structure, Photonics and Nanostructures-Fundamentals and Applications 23 (2017) 7–11.

[12] B. Wang, J. Rodríguez, M. A. Cappelli, 3d woodpile structure tunable plasma photonic crystal, Plasma Sources Science and Technology 28 (2) (2019) 02LT01.

[13] P. Moongkhamklang, V. Deshpande, H. Wadley, The compressive and shear response of titanium matrix composite lattice structures, Acta Materialia 58 (8) (2010) 2822–2835.

[14] Y. Liu, Z. Dong, J. Liang, J. Ge, Determination of the strength of a multilayer bcc lattice structure with face sheets, International Journal of Mechanical Sciences 152 (2019) 568–575.

[15] W. Yang, J. An, C. K. Chua, K. Zhou, Acoustic absorptions of multifunctional polymeric cellular structures based on triply periodic minimal surfaces fabricated by stereolithography, Virtual and Physical Prototyping 15 (2) (2020) 242–249.

[16] M. Ziminska, N. Dunne, A. R. Hamilton, Porous materials with tunable structure and mechanical properties via templated layer-by-layer assembly, ACS Applied Materials & Interfaces 8 (34) (2016) 21968–21973.

[17] S. Yang, K.-F. Leong, Z. Du, C.-K. Chua, The design of scaffolds for use in tissue engineering. part ii. rapid prototyping techniques, Tissue engineering 8 (1) (2002) 1–11.

[18] S. A. Yavari, M. Croes, B. Akhavan, F. Jahanmard, C. Eigenhuis, S. Dadbakhsh, H. Vogely, M. Bilek, A. Fluit, C. Boel, et al., Layer by layer coating for bio-functionalization of additively manufactured meta-biomaterials, Additive Manufacturing 32 (2020) 100991.

[19] K. Evans, Tensile network microstructures exhibiting negative poisson's ratios, Journal of Physics D: Applied Physics 22 (12) (1989) 1870.

[20] W. Warren, A. Kraynik, The linear elastic properties of open-cell foams (1988).

[21] R. Lakes, Foam structures with a negative poisson's ratio, Science 235 (1987) 1038–1041.

[22] L. J. Gibson, M. F. Ashby, Cellular solids: structure and properties, Cambridge university press, 1999.

[23] L. J. Gibson, M. F. Ashby, G. Schajer, C. Robertson, The mechanics of two-dimensional cellular materials, Proceedings of the Royal Society of London. A. Mathematical and Physical Sciences 382 (1782) (1982) 25–42.

[24] I. Gibson, M. F. Ashby, The mechanics of three-dimensional cellular materials, Proceedings of the Royal Society of London. A. Mathematical and Physical Sciences 382 (1782) (1982) 43–59.

[25] A. Bonfanti, A. Bhaskar, M. Ashby, Plastic deformation of cellular materials (2016).

[26] A. Bonfanti, A. Bhaskar, Elastoplastic response and recoil of honeycomb lattices, European Journal of Mechanics-A/Solids 71 (2018) 77–88.

[27] A. Bonfanti, S. Syngellakis, A. Bhaskar, Structural analysis of cyclically periodic rings and its application to the mechanics of balloon expandable stents, International Journal of Solids and Structures 185 (2020) 46–56.

[28] R. Christensen, Mechanics of low density materials, Journal of the Mechanics and Physics of Solids 34 (6) (1986) 563–578.

[29] M. Warner, S. Edwards, A scaling approach to elasticity and flow in solid foams, EPL (Europhysics Letters) 5 (7) (1988) 623.

[30] E. Cuan-Urquizo, A. Bhaskar, Flexural elasticity of woodpile lattice beams, European Journal of Mechanics-A/Solids 67 (2018) 187–199.

[31] S.-H. Ahn, M. Montero, D. Odell, S. Roundy, P. K. Wright, Anisotropic material properties of fused deposition modeling abs, Rapid Prototyping Journal 8 (4) (2002) 248–257.

[32] G. D. Goh, Y. L. Yap, H. Tan, S. L. Sing, G. L. Goh, W. Y. Yeong, Process–structure–properties in polymer additive manufacturing via material extrusion: A review, Critical Reviews in Solid State and Materials Sciences 45 (2) (2020) 113–133.

[33] J. Huang, Q. Chen, H. Jiang, B. Zou, L. Li, J. Liu, H. Yu, A survey of design methods for material extrusion polymer 3d printing, Virtual and Physical Prototyping 15 (2) (2020) 148–162.

[34] D. W. Hutmacher, T. Schantz, I. Zein, K. W. Ng, S. H. Teoh, K. C. Tan, Mechanical properties and cell cultural response of polycaprolactone scaffolds designed and fabricated via fused deposition modeling, Journal of biomedical materials research 55 (2) (2001) 203–216.

[35] I. Zein, D. W. Hutmacher, K. C. Tan, S. H. Teoh, Fused deposition modeling of novel scaffold architectures for tissue engineering applications, Biomaterials 23 (4) (2002) 1169–1185.

[36] P. Miranda, A. Pajares, E. Saiz, A. P. Tomsia, F. Guiberteau, Fracture modes under uniaxial compression in hydroxyapatite scaffolds fabricated by robocasting, J. Biomedical Materials Wiley InterScience Periodicals 83A (2007) 646–655.

[37] P. Miranda, A. Pajares, F. Guiberteau, Finite element modeling as a tool for predicting the fracture behavior of robocast scaffolds 4 (2008) 1715–1724.

[38] S. Naghieh, M. K. Ravari, M. Badrossamay, E. Foroozmehr, M. Kadkhodaei, Numerical investigation of the mechanical properties of the additive manufactured bone scaffolds fabricated by fdm: The effect of layer penetration and post-heating, Journal of the mechanical behavior of biomedical materials 59 (2016) 241–250.

[39] J. Norato, A. W. Johnson, A computational and cellular solids approach to the stiffness-based design of bone scaffolds, Journal of biomechanical engineering 133 (9) (2011) 091003.

[40] J. Ni, H. Ling, S. Zhang, Z. Wang, Z. Peng, C. Benyshek, R. Zan, A. K. Miri, Z. Li, X. Zhang, et al., Three-dimensional printing of metals for biomedical applications, Materials Today Bio (2019) 100024.

[41] S. Zhang, S. Vijayavenkataraman, W. F. Lu, J. Y. Fuh, A review on the use of computational methods to characterize, design, and optimize tissue engineering scaffolds, with a potential in 3d printing fabrication, Journal of Biomedical Materials Research Part B: Applied Biomaterials 107 (5) (2019) 1329–1351.

[42] J. M. Sobral, S. G. Caridade, R. A. Sousa, J. F. Mano, R. L. Reis, Three-dimensional plotted scaffolds with controlled pore size gradients: effect of scaffold geometry on mechanical performance and cell seeding efficiency, Acta Biomaterialia 7 (3) (2011) 1009–1018.

[43] M. Yeo, C. G. Simon, G. Kim, Effects of offset values of solid freeform fabricated pcl–β-tcp scaffolds on mechanical properties and cellular activities in bone tissue regeneration, Journal of Materials Chemistry 22 (40) (2012) 21636–21646.

[44] M. Afshar, A. P. Anaraki, H. Montazerian, J. Kadkhodapour, Additive manufacturing and mechanical characterization of graded porosity scaffolds designed based on triply periodic minimal surface architectures, Journal of the Mechanical Behavior of Biomedical Materials 62 (2016) 481–494.

[45] M. Too, K. Leong, C. Chua, Z. Du, S. Yang, C. Cheah, S. Ho, Investigation of 3D non-random porous structures by fused deposition modelling, The International Journal of Advanced Manufacturing Technology 19 (3) (2002) 217–223.

[46] T. Serra, J. A. Planell, M. Navarro, High-resolution pla-based composite scaffolds via 3-D printing technology, Acta biomaterialia 9 (3) (2013) 5521–5530.

[47] W. Wu, P. Geng, G. Li, D. Zhao, H. Zhang, J. Zhao, Influence of layer thickness and raster angle on the mechanical properties of 3D-printed PEEK and a comparative mechanical study between PEEK and ABS, Materials 8 (9) (2015) 5834–5846.

[48] F. J. Martínez-Vázquez, P. Miranda, F. Guiberteau, A. Pajares, Reinforcing bioceramic scaffolds with in situ synthesized ε-polycaprolactone coatings, Journal of Biomedical Materials Research Part A 101 (12) (2013) 3551–3559.

[49] R. Hedayati, M. Sadighi, M. Mohammadi Aghdam, A. Zadpoor, Mechanical properties of additively manufactured thick honeycombs, Materials 9 (8) (2016) 613.

[50] M. Jamshidian, E. A. Tehrany, M. Imran, M. Jacquot, S. Desobry, Poly-lactic acid: production, applications, nanocomposites, and release studies, Comprehensive Reviews in Food Science and Food Safety 9 (5) (2010) 552–571.

[51] J. M. Gere, S. Timoshenko, Mechanics of materials, Cole, Pacific Grove, CA (2001) 815–39.

[52] D. Systmes, Abaqus 6.11 analysis user's manual, Online Documentation Help (2013).

[53] E. Cuan-Urquizo, S. Yang, A. Bhaskar, Mechanical characterisation of additively manufactured material having lattice microstructure, in: IOP Conference Series: Materials Science and Engineering, Vol. 74, IOP Publishing, 2015, p. 012004.

[54] H. L. Langhaar, Dimensional analysis and theory of models, Vol. 2, Wiley New York, 1951.

[55] G. I. Barenblatt, B. G. Isaakovich, Scaling, self-similarity, and intermediate asymptotics: dimensional analysis and intermediate asymptotics, Vol. 14, Cambridge University Press, 1996.

[56] E. Buckingham, On physically similar systems; illustrations of the use of dimensional equations, Physical review 4 (4) (1914) 345.

Appendix

The eight algebraic equations resulting from the application of the boundary conditions are organised in the matrix form $\mathbf{Kx} = \mathbf{f}$, the coefficient matrix is given by

$$\mathbf{K} = \begin{bmatrix} 1 & 0 & 0 & 0 & 0 & 0 & 0 & 0 \\ 0 & 0 & 0 & 0 & 1 & (1-\alpha)\lambda & (1-\alpha)^2\lambda^2 & (1-\alpha)^3\lambda^3 \\ 0 & 1 & 0 & 0 & 0 & -1 & -2(1-\alpha)\lambda & -3(1-\alpha)^2\lambda^2 \\ 0 & 0 & 1 & 0 & 0 & 0 & -1 & -3(1-\alpha)\lambda \\ 1 & \alpha\lambda & \alpha^2\lambda^2 & \alpha^3\lambda^3 & -1 & 0 & 0 & 0 \\ 0 & 1 & 2\alpha\lambda & 3\alpha^2\lambda^2 & 0 & -1 & 0 & 0 \\ 0 & 0 & 1 & 3\alpha\lambda & 0 & 0 & -1 & 0 \\ 0 & 0 & 0 & 1 & 0 & 0 & 0 & -1 \end{bmatrix}. \tag{A1}$$

The eight unknowns are obtained as follow by applying boundary condition.

$$a_0 = 0, \tag{A2a}$$

$$a_1 = -\frac{F\lambda^2}{12EI}\left(2\alpha^3 - 3\alpha^2 + \alpha\right), \tag{A2b}$$

$$a_2 = \frac{F\lambda}{4EI}\left(\alpha^2 - \alpha\right), \tag{A2c}$$

$$a_3 = \frac{F}{6EI}\left(1-\alpha\right), \tag{A2d}$$

$$b_0 = -\frac{F\lambda^3}{12EI}\left(\alpha^2(1-\alpha)^2\right), \tag{A2e}$$

$$b_1 = -\frac{F\lambda^2}{12EI}\left(2\alpha^3 - 3\alpha^2 + \alpha\right), \tag{A2f}$$

$$b_2 = -\frac{F\lambda}{4EI}\left(\alpha^2 - \alpha\right), \tag{A2g}$$

$$b_3 = -\frac{F}{6EI}\alpha. \tag{A2h}$$

Displacement profile of a simply supported beam with length x.

$$w_{1,\mathrm{S}} = -\frac{F}{6EI}[(1-\alpha)(\alpha\lambda(2-\alpha)-x^2)] \quad 0 < x \leq \alpha\lambda \tag{A3a}$$

$$w_{2,\mathrm{S}} = -\frac{F}{6EI}\left[(1-\alpha)(\alpha\lambda(2-\alpha)-x^2)x + (x-\alpha\lambda)^3\right] \quad \alpha\lambda \leq x < \lambda \tag{A3b}$$

Displacement profile of a clamped beam with length x.

$$w_{1,\mathrm{C}} = -\frac{F}{6EI}\left[x^2(1-\alpha)(2\alpha(\lambda-x)+\alpha\lambda-x)\right] \quad 0 < x \leq \alpha\lambda \tag{A4a}$$

$$w_{2,\mathrm{C}} = -\frac{F}{6EI}\left[\alpha^2(\lambda-x)^2(2(1-\alpha)(2\alpha\lambda+x)+x-\alpha\lambda)\right] \quad \alpha\lambda \leq x < \lambda \tag{A4b}$$